

Article

## Effect of Particle Size and Operating Conditions on Pt<sub>3</sub>Co PEMFC Cathode Catalyst Durability

Mallika Gummalla <sup>1</sup>, Sarah C. Ball <sup>2</sup>, David A. Condit <sup>1,†</sup>, Somaye Rasouli <sup>3</sup>, Kang Yu <sup>3</sup>, Paulo J. Ferreira <sup>3</sup>, Deborah J. Myers <sup>4</sup> and Zhiwei Yang <sup>1,\*</sup>

<sup>1</sup> United Technologies Research Center, East Hartford, CT 06108, USA;

E-Mail: GummalM@utrc.utc.com

<sup>2</sup> Johnson Matthey Technology Centre, Blounts Court, Sonning Common, Reading RG4 9NH, UK;

E-Mail: ballsc@matthey.com

<sup>3</sup> Materials Science and Engineering Program, University of Texas, Austin, TX 78712, USA;

E-Mails: ss.rasouli@gmail.com (S.R.); kangyu@utexas.edu (K.Y.);

ferreira@mail.utexas.edu (P.J.F.)

<sup>4</sup> Chemical Sciences and Engineering Division, Argonne National Laboratory, Lemont, IL 60439,

USA; E-Mail: dmyers@anl.gov

† This author deceased on 4 June 2014.

\* Author to whom correspondence should be addressed; E-Mail: yangz@utrc.utc.com;

Tel.: +1-860-610-7247; Fax: +1-860-660-6724.

Academic Editor: Minhua Shao

Received: 25 April 2015 / Accepted: 21 May 2015 / Published: 29 May 2015

---

**Abstract:** The initial performance and decay trends of polymer electrolyte membrane fuel cells (PEMFC) cathodes with Pt<sub>3</sub>Co catalysts of three mean particle sizes (4.9 nm, 8.1 nm, and 14.8 nm) with identical Pt loadings are compared. Even though the cathode based on 4.9 nm catalyst exhibited the highest initial electrochemical surface area (ECA) and mass activity, the cathode based on 8.1 nm catalyst showed better initial performance at high currents. Owing to the low mass activity of the large particles, the initial performance of the 14.8 nm Pt<sub>3</sub>Co-based electrode was the lowest. The performance decay rate of the electrodes with the smallest Pt<sub>3</sub>Co particle size was the highest and that of the largest Pt<sub>3</sub>Co particle size was lowest. Interestingly, with increasing number of decay cycles (0.6 to 1.0 V, 50 mV/s), the relative improvement in performance of the cathode based on 8.1 nm Pt<sub>3</sub>Co over the 4.9 nm Pt<sub>3</sub>Co increased, owing to better stability of the 8.1 nm catalyst. The electron

microprobe analysis (EMPA) of the decayed membrane-electrode assembly (MEA) showed that the amount of Co in the membrane was lower for the larger particles, and the platinum loss into the membrane also decreased with increasing particle size. This suggests that the higher initial performance at high currents with 8.1 nm Pt<sub>3</sub>Co could be due to lower contamination of the ionomer in the electrode. Furthermore, lower loss of Co from the catalyst with increased particle size could be one of the factors contributing to the stability of ECA and mass activity of electrodes with larger cathode catalyst particles. To delineate the impact of particle size and alloy effects, these results are compared with prior work from our research group on size effects of pure platinum catalysts. The impact of PEMFC operating conditions, including upper potential, relative humidity, and temperature on the alloy catalyst decay trends, along with the EMPA analysis of the decayed MEAs, are reported.

**Keywords:** Pt<sub>3</sub>Co catalyst; PEM fuel cells; in-cell performance; catalyst durability

---

## 1. Introduction

To reduce the electrocatalyst cost for polymer electrolyte membrane fuel cells (PEMFCs), platinum alloys with higher oxygen reduction reaction (ORR) mass activity are being developed. In particular, alloys such as Pt<sub>3</sub>Co, Pt<sub>3</sub>Fe and Pt<sub>3</sub>Ni have been shown to provide higher ORR mass activity (A/g-Pt) and specific activity (mA/cm<sup>2</sup>-Pt) than pure Pt catalysts [1–3]. In aqueous environments, the rotating disk electrode (RDE) measurements found that polycrystalline Pt<sub>3</sub>Co with a Pt skin has ORR specific activity three times greater than pure Pt, and Pt<sub>3</sub>Ni(111) has the highest ORR specific activity recorded to date with an enhancement factor of nearly twenty *versus* polycrystalline Pt [2,4,5]. Additionally, in RDE measurements, carbon-supported nanoparticles of Pt<sub>3</sub>Co with a mean diameter of 6 nm showed an ORR specific activity enhancement factor of three *versus* 6 nm mean diameter Pt [6]. Paulus *et al.* found that Pt based alloy catalysts exhibit higher ORR specific activity than pure Pt by an enhancement factor of approximately 1.5 for bulk electrodes, 1.5 to 2 for supported Pt<sub>3</sub>X catalysts, and 2 to 3 for PtCo catalyst [7]. There are relatively few measurements of ORR activity for Pt alloys in the fuel cell environment. In a study where Co, Ni and Fe-based Pt alloy catalysts were evaluated in a fuel cell, the initial mass activity was found to be the highest for the Pt–Fe catalyst and lowest for pure Pt catalyst [2,3]. Recently, Huang *et al.* demonstrated an ORR specific activity enhancement factor of 3.5 in the fuel cell environment for Pt<sub>3</sub>Co/Ketjen carbon *versus* Pt/Vulcan carbon, albeit for different particle sizes [8].

The enhancement in ORR activity observed for Pt alloys *versus* Pt has been attributed to modification of the electronic/atomic structure of the alloy catalyst surface [2,4,9–12]. Using X-ray absorption near edge structure (XANES), Min *et al.* showed that the structure sensitivity is associated with the adsorption strength of oxygen intermediates on the Pt surface [13,14]. Furthermore, they reported that the reduced Pt–Pt neighbor distance on the surface of the alloy catalysts is favorable for the adsorption of oxygen. Through experimental and theoretical studies, Mukerjee *et al.* suggested that this improvement can be attributed to a positive shift of the onset potential for forming OH<sub>ads</sub> on the alloy

relative to the Pt catalyst, thereby allowing O<sub>2</sub> to adsorb at higher potentials and reducing the overpotential for O<sub>2</sub> reduction [14,15].

Degradation studies of Pt<sub>3</sub>Co alloys in a 16 cell stack showed that Co leaches out, at the nanometer scale, resulting in a “Pt skeleton” structure at the topmost surface layer of Pt<sub>3</sub>Co particles within the first hour of operation. With longer operational time, the particles slowly evolve toward “Pt-shell/Pt–Co alloy core” structures with depleted Co content and a Pt-enriched shell (of the order of two atomic monolayers after 1124 h of operation) due to Co surface segregation/leaching and Ostwald ripening [16,17]. Chen *et al.* showed that the acid treated Pt<sub>x</sub>Co resulted in Co dissolution, which increased the thickness of the Pt-enriched surface layer. This structural change was identified as a contributor to the reduction in the specific activity of Pt<sub>x</sub>Co nanoparticles after potential cycling [18]. Popov *et al.* reported that pure Pt catalyst showed higher ECA decay rate than that of Pt<sub>3</sub>Co catalyst during potential cycling in acidic aqueous environment as well as during constant current holding in-cell test, however the initial particle sizes of Pt is lower than that of Pt<sub>3</sub>Co in this comparison [3].

Shao *et al.* have shown through systematic synthesis of mono-dispersed Pt catalysts that the catalytic activity depends on the shape and size of the nanoparticles [19]. Furthermore it is reported that the edge sites, which increase in fraction of total surface sites with decreasing particle size, have lower specific activity due to very strong oxygen binding energies [19–22]. Even with the same alloy metal combinations, the particle size effects are difficult to delineate as the heat treatment used to increase particle size results in a varied degree of alloying, and, thus, different surface activity [23,24]. Pt-alone and Pt-based alloy catalysts both show increasing ORR specific activities with decreasing specific surface area (*i.e.*, increasing particle size) [25–29].

As the heat treatment temperature is increased the degree of alloying increases along with the particle size. Min *et al.* showed that the particle size and alloying effects are the two most important factors affecting the catalytic activity towards ORR, with lowered Pt–Pt bond distance resulting in favorable adsorption of oxygen [13]. The recent work by Matsutani *et al.* reported particle size effects of the Pt and PtCo catalyst performance in MEAs and suggested that the MEAs with cathodes containing 4–5 nm Pt particles and 7–8 nm PtCo particles were the most stable. These two sizes were the largest of the catalyst particles studied [30]. These catalysts were found to be more stable when heat treated to a higher temperature. However, the heat treatment conditions changed the PtCo composition along with particle size. This leaves an unanswered question about the factor impacting durability, namely whether it is the size, the composition, or a combination of these two factors. The impact of Pt<sub>3</sub>Co particle size with nearly identical metal ratio is needed to delineate the effects of composition and particle size on the initial performance and stability.

The catalyst structures, such as the core-shell type, offer the benefits of low platinum content in the electrodes and high activity [31–34]. However, the core-shell catalysts are large and often in the size range of 10 nm. To elucidate the role of these new catalyst structures, the contribution of the alloy and size effects needs to be understood. Recently, our research group has shown that the activity and stability of the Pt catalysts in an MEA is strongly dependent on the particle size, and an optimum particle size between 3.2 and 7.1 nm is suggested for maximized life averaged performance per mg Pt [35]. The focus of this paper is to report a similar systematic analysis of Pt<sub>3</sub>Co catalysts that have nearly identical metal ratio but different mean particle sizes, and contrast these with Pt catalysts to delineate the impact of alloying and particle size.

## 2. Results and Discussion

Pt<sub>3</sub>Co catalysts with nearly identical Pt:Co:carbon ratio (shown in Table 1) but different mean particle sizes were prepared by heat treatment, in order to distinguish the effects of composition from particle size on the initial performance and stability. While, in spite of nearly identical Pt:Co metal ratio, as verified by ICP-OES and X-ray fluorescence measurements, the Pt<sub>3</sub>Co catalysts with different particle sizes are ineluctably associated with variance, to some extent, in the degree of alloy ordering, which is shown in the X-ray diffraction patterns (Figure 1). The superlattice reflections appear to be clearer for larger particle sizes, indicating a higher degree of ordering.

**Table 1.** Characterization of Pt<sub>3</sub>Co/Ketjen EC 300J catalysts tested.

Sample	wt.% Pt	wt.% Co	XRD crystallite Size (nm)	XRD L.P (Å)	CO area (m <sup>2</sup> /g-Pt)	TEM mean diameter (nm)	St error	N
1	37.9	3.88	3.9	3.848	35	4.9	0.2	200
2	38.5	3.94	5.6	3.850	23	8.1	0.3	200
3	38.4	3.93	9.5	3.850	11.3	14.8	0.6	200

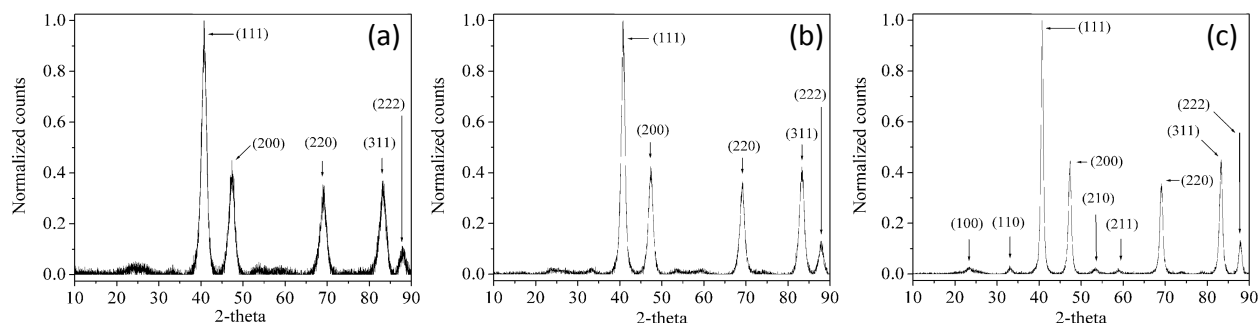


**Figure 1.** X-ray diffraction patterns of as prepared (a) 4.9 nm (b) 8.1 nm and (c) 14.8 nm Pt<sub>3</sub>Co on carbon powders.

Systematic tests carried out on the Pt<sub>3</sub>Co catalysts for particle size study are listed in Table 2, while Table 3 shows the tests performed at different operating conditions for the parametric study. The electrodes with small Pt<sub>3</sub>Co particle size (4.9 nm) were used for the parametric study in order to better distinguish the difference of the operating condition impact on cells' performance degradation. The ECAs of the cathodes reported in Table 2 are the peak ECAs observed between 0–1000 potential cycles. All ECAs in this study were characterized using the hydrogen absorption area in the CV. In general, these calculated ECA values may underestimate the catalysts' real electrochemical surface areas to some extent, due to the possible disruptive influences such as hydrogen evolution and the difference of catalyst surface structures [36–38]. However, in this study, since the MEA tests were carried out with the same protocol and the CVs were performed under the identical temperature, RH, and gas flow rate conditions, these calculated ECA values are meaningful for the comparison purpose and revealing the ECA evolution trend along the potential decay cycling. As expected, the values showed the trend of decreasing ECAs with increasing catalyst mean particle size.

**Table 2.** Pt<sub>3</sub>Co catalyst particle sizes used in this study and cycling conditions used to test their electrochemical stability. Note that the ECA values reported are the peak ECA's.

Cell #	Mean diameter (nm) (ECA, m <sup>2</sup> /g-Pt)	Anode/cathode Pt loading mg-Pt/cm <sup>2</sup>	Potential cycling conditions
1	4.9 (37)	0.19/0.23	Triangle wave potential cycle: 0.6 V to 1.0 V (50 mV/s ramp rate) Cell Temperature: 80 °C Humidity: Anode = Cathode = 100% RH Fuel/Oxidant: H <sub>2</sub> at 100 sccm/N <sub>2</sub> at 50 sccm Pressure: Atmospheric pressure
1a *	4.9 (40)	0.22/0.18	
2	8.1 (27)	0.20/0.22	
3	14.8 (23)	0.20/0.22	

\* The cathode Pt<sub>3</sub>Co catalyst was pre-leached.

**Table 3.** Operating conditions used for testing the electrochemical stability of the 4.9 nm Pt<sub>3</sub>Co catalysts.

Cell #	Description	Potential cycling conditions
4	Baseline	Square wave potential cycle: 10 s at 0.4 V, 10 s at 0.95 V (20 s/cycle) Cell Temperature: 80 °C Humidity: Anode = Cathode = 100% RH Fuel/Oxidant: 0.5 SPLM 4% H <sub>2</sub> /0.5 SPLM N <sub>2</sub> Pressure: Atmospheric pressure
5	Lower RH	Humidity: Anode = Cathode = 30% RH All other parameters were same as 4 #
6	Higher Upper Potential	Square wave potential cycle: 10 s at 0.4 V, 10 s at 1.05 V (20 s/cycle) All other parameters were same as 4 #
7	Higher Temperature	Cell Temperature: 90 °C All other parameters were same as 4 #

The beginning of life (BOL) performance curves for cells 1–3 are shown in Figure 2 for H<sub>2</sub>/O<sub>2</sub> (a) and for H<sub>2</sub>/air (b) using the test conditions described in the cell performance section. The V-I performance curves reported here are corrected for the membrane resistance (*i.e.*, IR-corrected) to allow analysis of the electrode changes. The performance of the 4.9 nm Pt<sub>3</sub>Co electrode in O<sub>2</sub> is slightly higher than the 8.1 nm Pt<sub>3</sub>Co electrode at current densities <400 mA/cm<sup>2</sup> (e.g., ~8 mV at 40 mA/cm<sup>2</sup>), however there is no noticeable voltage benefit at higher current densities under H<sub>2</sub>/O<sub>2</sub> condition. Interestingly, the performance of the 8.1 nm electrode provided ~17 mV higher performance than the 4.9 nm Pt<sub>3</sub>Co electrode at 1.5 A/cm<sup>2</sup> under H<sub>2</sub>/air conditions. The 14.8 nm Pt<sub>3</sub>Co electrode resulted in a V-I performance that is significantly lower, indicating lower mass activity and/or higher electrode resistance to proton transport. In this study, the catalyst loading was maintained at ~0.2 mg Pt/cm<sup>2</sup> for all electrodes. In an idealized case of spherical particles of uniform particle size, the distance between the particles is expected to scale as  $d^{1.5}$ , where  $d$  is the diameter of the particle. This suggests that the 4.9 nm Pt<sub>3</sub>Co particles on the carbon support would be ~2 times closer to each other (using the metric of geometric distance) than the 8.1 nm Pt<sub>3</sub>Co particles and ~4 times closer when compared to the 14.8 nm particles. Fewer particles in electrodes could result in fewer access points for ORR, and lower net

oxygen concentration at the catalyst surface, resulting in lower performance with larger particles [39]. The effect of this catalyst particle spacing is expected to be greater on the performance in air than in oxygen, as seen in Figure 2.

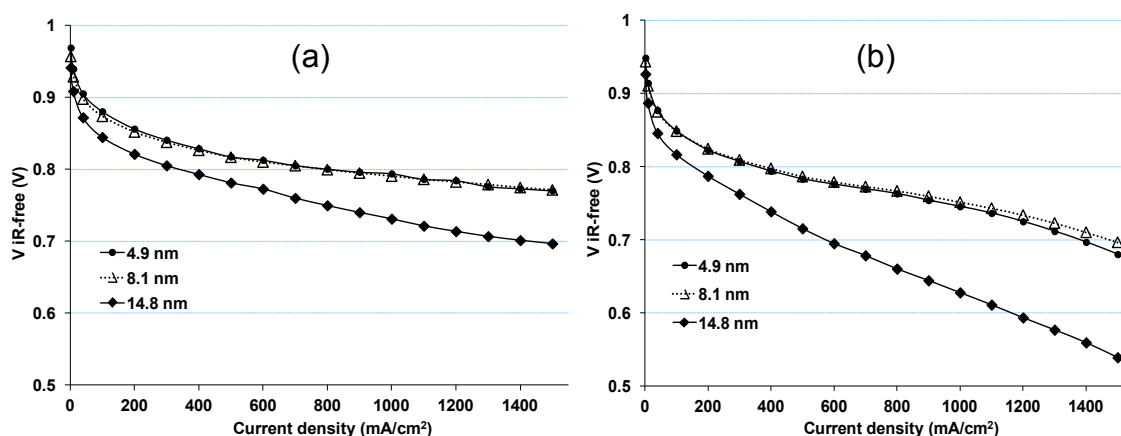


**Figure 2.** The beginning of life V-I performance of 4.9, 8.1, and 14.8 nm Pt<sub>3</sub>Co catalyst based MEAs, H<sub>2</sub>/O<sub>2</sub> (a) and H<sub>2</sub>/Air (b).

The H<sub>2</sub>/O<sub>2</sub> performance suggests that the electrode ionic resistance is higher for the electrode with the larger catalyst particles (*i.e.*, 14.8 nm Pt<sub>3</sub>Co). While, comparing to the 8.1 nm Pt<sub>3</sub>Co catalyst-based electrode, the 4.9 nm Pt<sub>3</sub>Co catalyst-based electrode also shows slightly higher electrode resistance, which could be due to the increased fraction of cobalt in the ionomer [40]. Decreasing the amount of easily removable Co from the alloy by pre-leaching may decrease the Co content in the ionomer. Hence, a pre-leached 4.9 nm Pt<sub>3</sub>Co catalyst-based MEA was also tested. The results are shown in Figure 3. The Pt loading in the pre-leached catalyst-based electrode was ~20% lower than the as-made catalyst-based electrode, hence lower performance is seen in the low current regions. The comparison of the H<sub>2</sub>/O<sub>2</sub> performance curves shows that the slope in the middle-high current region is lower for the pre-leached catalysts, suggesting lower ionic resistance in the electrode. The lower Co content in the electrode with the pre-leached catalysts is likely to be the factor for the improved performance observed in the high current region of the H<sub>2</sub>/air polarization curve. In summary, both MEAs with as-made large and small Pt<sub>3</sub>Co particle sizes showed lower performance at high current region for different reasons; the 4.9 nm Pt<sub>3</sub>Co MEAs were likely to have higher Co contamination and the 14.7 nm Pt<sub>3</sub>Co MEAs were likely to have higher local oxygen transport resistance issue.

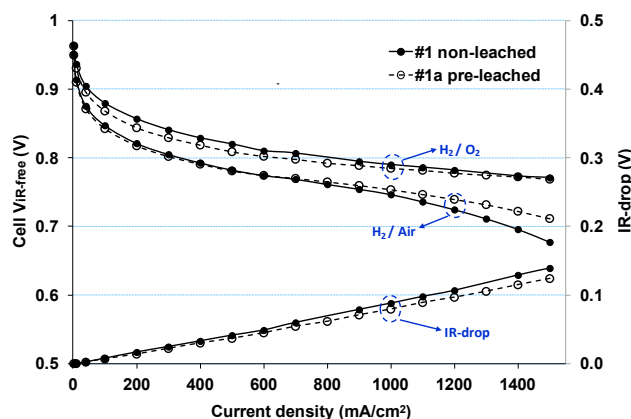


**Figure 3.** The beginning of life V-I performance of pre-leached and as made 4.9 nm Pt<sub>3</sub>Co catalyst based MEAs.

### 2.1. Impact of Catalyst Particle Size on Cell Performance Degradation

The decay characteristics of the four Pt<sub>3</sub>Co electrodes are tracked by monitoring the ECA, mass activity, and H<sub>2</sub>/Air performance at 0.8 A/cm<sup>2</sup> and 1.5 A/cm<sup>2</sup>. Figure 4a shows the trends of ECA evolution, in which the ECA for 4.9 nm Pt<sub>3</sub>Co generally decreases from 1000 to 30,000 cycles while the ECA for the larger particles, 8.1 nm and 14.8 nm, stabilizes after 3000 to 5000 cycles. The smaller particle electrodes exhibited higher initial ECA values as expected, owing to a higher surface area per unit mass. The mass activity decay trends capture the evolution of the catalyst activity for ORR with minimal disturbance from oxygen transport and proton transport resistances. Figure 4b shows that the mass activity decay is highest for 4.9 nm Pt<sub>3</sub>Co particles and lowest for 14.8 nm Pt<sub>3</sub>Co particles. At the end of 30,000 cycles the MEA with 8.1 nm particle size retained higher mass activity than the MEAs containing the 4.9 nm and 14.8 nm Pt<sub>3</sub>Co particles. The relatively stable mass activity and ECA of the catalysts with larger particle sizes suggests minimal changes to the catalyst and to the electrode structure with cycling.

Figure 4c,d show the H<sub>2</sub>/Air performance during decay cycling of the four electrodes at 0.8 A/cm<sup>2</sup> and 1.5 A/cm<sup>2</sup>, respectively. While the performance of the 8.1 nm Pt<sub>3</sub>Co-based electrode improved slightly within the first 5000 cycles, significant improvement is seen in the case of the 14.8 nm Pt<sub>3</sub>Co-based electrode. This improvement may be attributed to further wet-up conditioning within the cathode from potential cycling and diagnostic tests, such as possibly improving the ionic contact within the electrode. The ORR specific activity calculated by dividing mass activity by the corresponding ECA shows to be higher for the 8.1 nm Pt<sub>3</sub>Co (0.89 mA/cm<sup>2</sup>-Pt) than the 4.9 nm Pt<sub>3</sub>Co (0.65 mA/cm<sup>2</sup>-Pt) at the BOL, and both of which generally decrease with the potential cycles. The ORR specific activity of the 14.8 nm Pt<sub>3</sub>Co shows to be the lowest (0.43 mA/cm<sup>2</sup>-Pt) at the BOL, which gains significant increase from potential cycling and peaks at 0.67 mA/cm<sup>2</sup>-Pt after the first 5000 cycles. At the end of 30,000 cycles, the ORR specific activities of 8.1 nm Pt<sub>3</sub>Co and 14.8 nm Pt<sub>3</sub>Co retain the same (0.61 mA/cm<sup>2</sup>-Pt) and are higher than that of 4.9 nm Pt<sub>3</sub>Co particles (0.52 mA/cm<sup>2</sup>-Pt).

It is clear from the cell performance trends shown in Figure 4 that 8.1 nm Pt<sub>3</sub>Co is significantly more durable than the 4.9 nm Pt<sub>3</sub>Co and provides significantly better performance than 14.8 nm Pt<sub>3</sub>Co throughout the kinetic and mass transport-limited regions. The decay trends of the pre-leached Pt<sub>3</sub>Co 4.9 nm

based electrode are also shown in Figure 4, with the dashed line. The performance decay rate of the pre-leached catalyst is higher than that observed for the non-leached catalyst of the same particle size. The detailed reason is unclear.

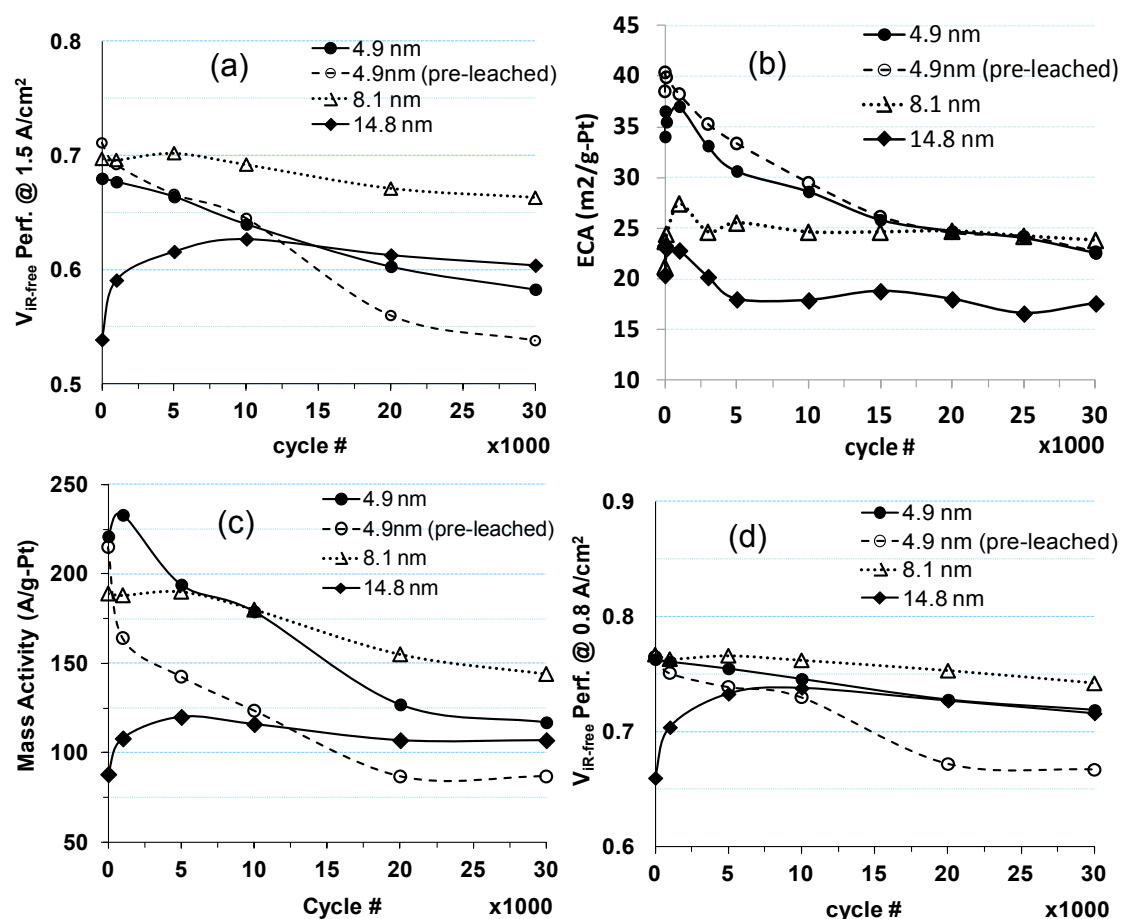


**Figure 4.** Performance decay with potential cycling for 4.9 nm, 8.1 nm, and 14.8 nm Pt<sub>3</sub>Co electrodes, (a) ECA, (b) Mass activity (A/g-Pt at 0.90 V), (c) H<sub>2</sub>/Air performance at 0.8 A/cm<sup>2</sup> and (d) H<sub>2</sub>/Air performance at 1.5 A/cm<sup>2</sup>.

The cross-section post-test EMPA analysis with Pt, S and Co profiling, shown in Figure 5, indicates that dissolution-precipitation occurs near the cathode-membrane interface where Pt<sup>2+/4+</sup> ions migrate from the cathode into the membrane to be reduced by crossover H<sub>2</sub>. A very distinct band of platinum close to the cathode/membrane interface is seen in all samples. The estimated fraction of platinum from the cathode that moved into the membrane after 30,000 cycles is shown in Table 4. The 4.9 nm Pt<sub>3</sub>Co-based electrode exhibited ~14% of platinum from the electrode lost to the membrane, while the other two electrodes lost less than 5%. The fraction of ECA lost for the 4.9 nm, 8.1 nm, and 14.8 nm Pt<sub>3</sub>Co based electrodes after 30,000 cycles was 39, 13, and 23%, respectively. The loss of platinum from the electrode was only a small contributor to the overall ECA and mass activity losses observed for these electrodes, thus, having insignificant impact on the overall ECA and mass activity decay trends in this study, though all ECAs and mass activities were calculated from the electrodes' initial Pt loading. It is important to note that some entrapment of air occurred during processing of the catalyst ionomer inks of the Pt<sub>3</sub>Co/C cathode materials used in this study leading to macroscopic porosity within

the electrodes of the final MEAs. The pores appear as dark lenticular features in the EMPA images although it should be noted that similar features can also be introduced during the sample preparation for the EMPA. Therefore, analysis of those features is not attempted in this article. The Co line scans shown in the top plots are re-plotted in the bottom plots with a more sensitive  $y$ -axis scale for clarity. The Co plots indicate that some  $\text{Co}^{n+}$  ions migrate into the membrane, but stop at the anode.  $\text{Co}^{n+}$  remains in a cationic form after the  $\text{Pt}_3\text{Co}$  dissolves while  $\text{Pt}^{2+/4+}$  is reduced to metallic Pt ( $\text{Pt}^0$ ) by crossover  $\text{H}_2$  within the cathode and membrane ionomer. An interesting observation from these plots is that the  $\text{Co}^{n+}$  wt.% in the membrane is greatest for the 4.9 nm non-leached case and lowest for the 14.8 nm case. The decreased  $\text{Co}^{n+}$  content in the membrane and electrode observed via EPMA for the pre-leached 4.9 nm  $\text{Pt}_3\text{Co}$  is consistent with the hypothesis presented earlier.

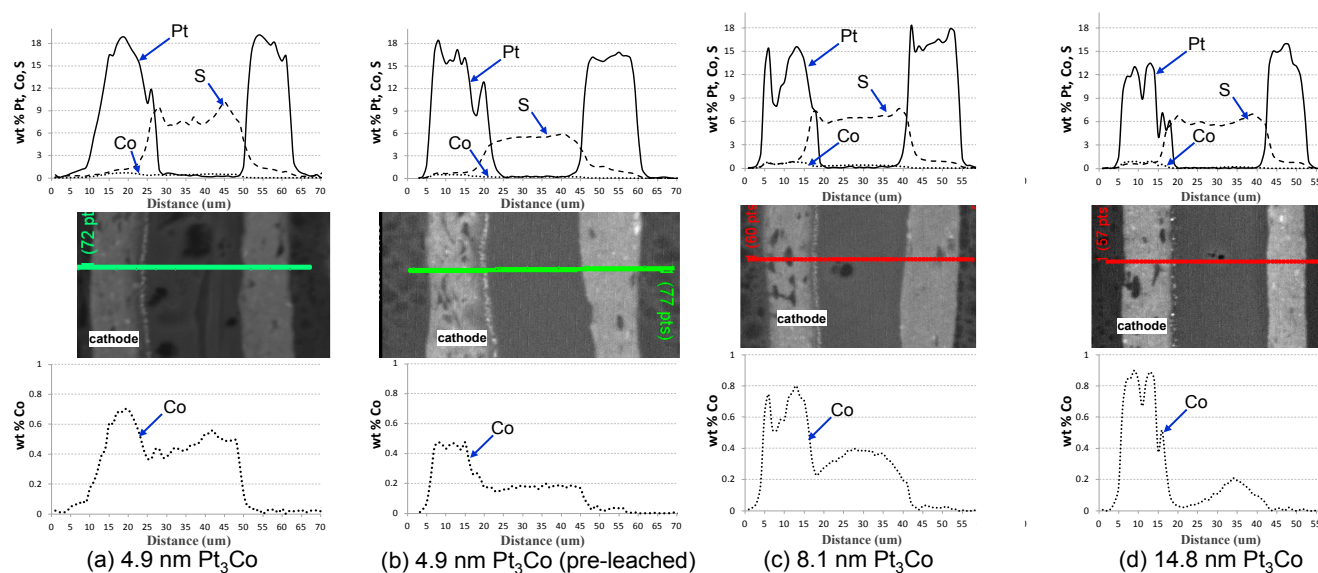


**Figure 5.** Post-test analysis of  $\text{Pt}_3\text{Co}$  particle size study at subscale cell plan form midpoint shows minor migration of Pt and Co into membrane.

**Table 4.** The loss of platinum calculated from EMPA, loss of cobalt calculated from the XRF, and post-cycling Pt to Co ratio in electrode from XRF after 30,000 cycles.

Cell #	Mean diameter (nm) (ECA, $\text{m}^2/\text{g-Pt}$ )	% of Pt lost into membrane	% Co most from electrode	Pt/Co ratio
1	4.9 (37)	$14.3 \pm 2\%$	63	8.4
2	8.1 (27)	$3.7 \pm 2\%$	45	5.5
3	14.8 (23)	$3.0 \pm 1\%$	30	4.2

The Pt to Co atomic ratios in the cathodes of the three cycled MEAs, as determined by XRF, are shown in Table 4. This ratio was found to decrease with increasing initial mean  $\text{Pt}_3\text{Co}$  size. This trend reflects decreased extent of Co leaching from the catalysts with increasing particle size, which is in agreement with the trend observed for wt.%  $\text{Co}^{n+}$  found in the membrane for the three different particle

sizes from the EMPA analysis. The observed trends in the particle size dependence of the fraction of Co lost from the catalysts can be understood in terms of the particle size dependence of the fraction of total atoms in a nanoparticle residing on the surface of the particles (*i.e.*, surface/volume  $\propto 1/d$ , where  $d$  is the diameter of the nanoparticle). Assuming that an insignificant amount of Pt lost from the catalyst particles relative to the amount of Co lost, and using the known data, including the initial and post-cycling Pt to Co ratios, the mean particle sizes, and the XRD-determined lattice spacing of the alloy (0.385 nm), the depth of Co loss from the topmost layers of the catalyst particles was calculated to be approximately one atomic layer for the pre-cycled electrodes and three atomic layers for the post-cycled electrodes. The results are in agreement with previous data [24,41,42]. The depth of de-alloying was found to be independent of the initial mean particle size of the catalysts.

To gain greater insight into the observed decay trends of MEAs with varied catalyst particle size, the TEM-based catalyst particle size distributions of the pre- and post-cycling electrodes are shown in Figure 6. The TEM results of the 4.9 nm based electrode, Figure 6a, shows significant tailing towards the larger particle sizes at the end of 30,000 decay cycles compared to the pristine catalyst. However, the changes in particle size distribution for the 8.1 nm and 14.8 nm are relatively insignificant with cycling (Figure 6b,c). These results suggest that the loss in mass activity observed for the 4.9 nm catalyst could be a combination of catalyst restructuring as well as particle size changes, while for the 8.1 and 14.8 nm catalysts, the origin of the losses may be primarily due to catalyst restructuring. Based on the literature data and the EMPA and the XRF data presented here, it can be speculated that the restructuring includes dissolution of Co from the Pt<sub>3</sub>Co particle surface and sub-layers and subsequent migration into cathode/membrane ionomer as Co<sup>n+</sup>. This may result in a Pt-rich shell encasing a Pt<sub>3</sub>Co core, explaining the enhanced ORR activity observed with Pt-Co alloys [24]. The TEM-derived particle size distributions also show that cycling caused the average particle size of the 14.8 nm catalyst to decrease by approximately 1.8 nm. The observed shrinkage of these particles indicates that there is minimal coarsening of these large particles such that the shrinkage of the particles due to loss of cobalt is observable. The further understanding of the catalysts surface restructuring at atomic level needs more comprehensive characterization which was not attempted in this study.

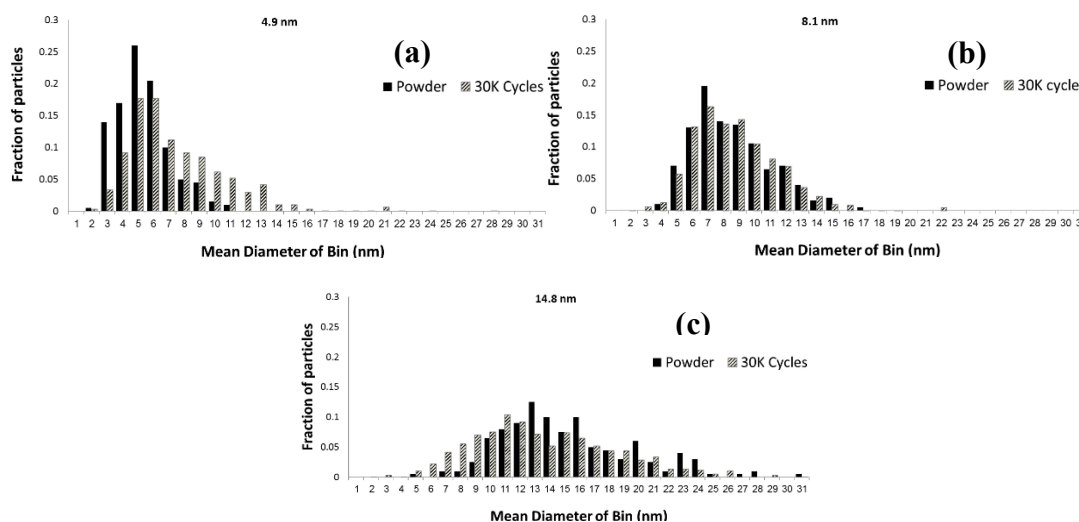


**Figure 6.** TEM analysis of Pt<sub>3</sub>Co particle size distribution of the pristine (**black**) and decayed MEAs (**hashed**), (a) 4.9 nm (b) 8.1 nm and (c) 14.8 nm Pt<sub>3</sub>Co supported on carbon.

The initial performance and decay trends of Pt<sub>3</sub>Co and Pt over a wide range of particle sizes are compared. The performance and decay characteristics of 1.9, 3.2, 7.1 and 12.3 nm Pt particle based-MEAs is reported in our prior work [35]. Figure 7 shows the mass activity, ECA, specific activity and high current performance of both Pt and Pt<sub>3</sub>Co-based MEAs along with the decay trends. The initial mass activity values of between 180 and 220 A/g-Pt measured for the 4.9 and 8.3 nm Pt<sub>3</sub>Co MEAs in this study are slightly lower than those reported previously on similar catalyst materials [1], however the overall trends are comparable, with a peak in mass activity at intermediate particle size and lower mass activity for the very large particles due to the reduced available metal area. The heat treatment conditions during catalyst preparation, the formulations and processes used in catalyst ink preparation, and MEA fabrication all have an important role to play in realizing the initial mass activity benefits reported in literature. Comparable procedures were used for both the Pt and Pt<sub>3</sub>Co materials in this study, however resulting data show greater improvements of Pt only performance over past data [1] compared to Pt<sub>3</sub>Co examples, bringing mass activity values closer for the two catalyst types in the current study.

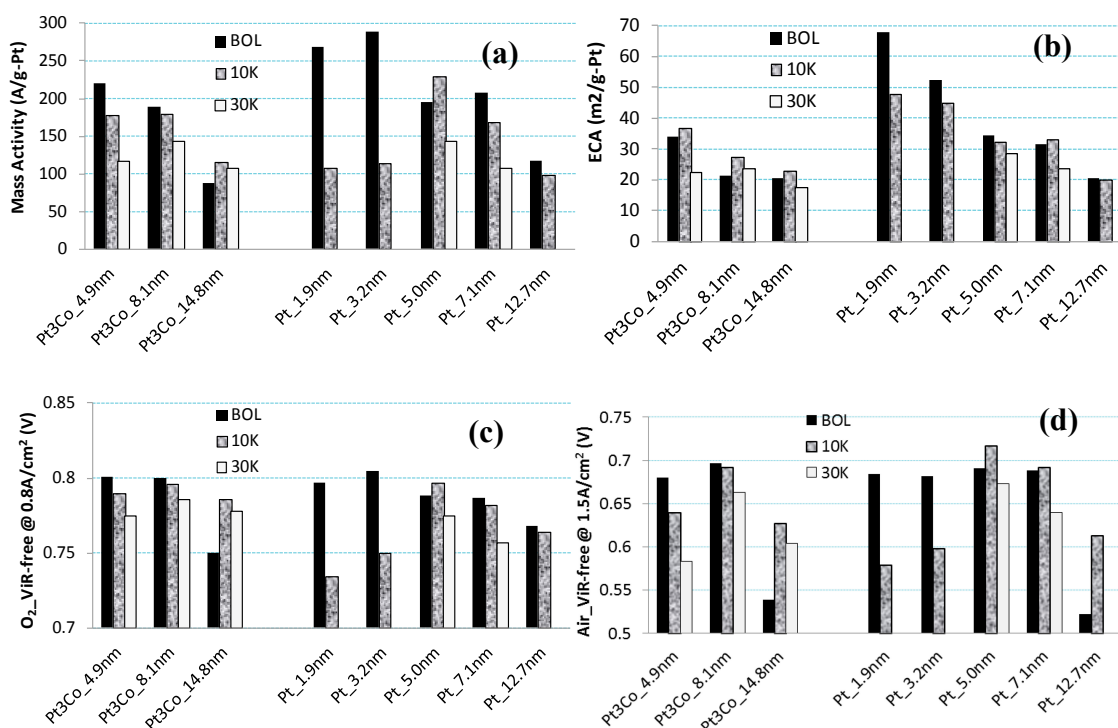


**Figure 7.** Comparison of Pt vs. Pt<sub>3</sub>Co decay trends as a function of potential cycles. (a) Mass Activity, (b) ECA, (c) H<sub>2</sub>/O<sub>2</sub> performance at 0.8 A/cm<sup>2</sup>, (d) H<sub>2</sub>/Air performance at 1.5 A/cm<sup>2</sup>.

The results are shown for initial and after 10,000 and 30,000 (when available) decay cycles. While the experimental errors make the decay rates hard to quantify with great accuracy, a few trends are clearly evident. The decay rate is catalyst size dependent with larger sized catalysts decaying slower. This is due to that larger nanoparticles have larger surface area and therefore better stability (Gibbs-Thompson effect) and larger nanoparticles (>10 nm) are more stable against agglomeration compared to the smaller particles. The mass activity data shown in Figure 7a indicates that the initial mass activity decreases with increase in particle size. However, the 10,000 and 30,000 mass activity data suggests that the best results are obtained with the 8.1 nm Pt<sub>3</sub>Co and 5 nm Pt. The ECA decay rate is lower for larger particle sizes as shown in Figure 7b, for both the Pt and Pt<sub>3</sub>Co catalysts. Figure 8c,d

show the performance at 0.8 A/cm<sup>2</sup> in H<sub>2</sub>/O<sub>2</sub> and 1.5 A/cm<sup>2</sup> in H<sub>2</sub>/air for all the cathode catalysts and sizes evaluated. A common trend observed is the initial performance of the largest particles is significantly lower than the smaller particle sizes. However, the performance improves during the 10,000 cycles and subsequently decreases. The intermediate size catalysts evaluated in this study provide the best end-of-life performance. In summary, the catalysts with initial mean diameters of ~5 to ~8.1 nm for both Pt and Pt<sub>3</sub>Co showed balanced performance and durability, giving the best overall life-averaged performance. For the Pt MEAs, that containing the 5 nm Pt was the best performer and most durable over 30,000 cycles. Analogously, 8.1 nm was the best performer for the Pt<sub>3</sub>Co MEAs, within the particle sizes studied.

## 2.2. Impact of Operating Conditions on Cell Performance Degradation

The parametric study of fuel cell operating conditions, for cells listed in Table 3, was performed with the 4.9 nm Pt<sub>3</sub>Co cathodes using a square wave potential cycle, 0.40–0.95V (vs. anode), which represents transients between peak and idle power for typical automotive FC operation. The anode was 4% H<sub>2</sub> (balance N<sub>2</sub>), which served as a stable reference to the square wave potential cycle imposed on the cathode. Low RH (30%) and high temperature (90 °C) are extreme operating conditions that may impact catalyst degradation. Higher upper potential (1.05 V vs. anode) can occur at high fuel utilization conditions and/or during startup/shutdown.

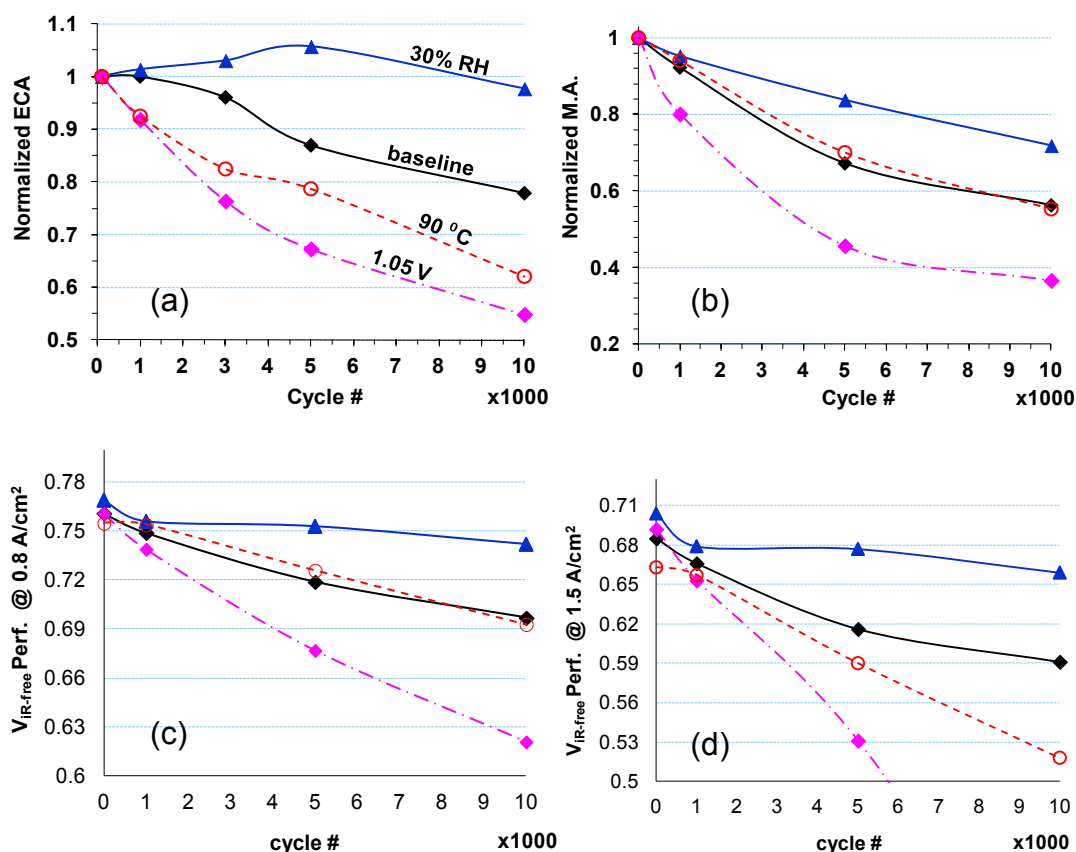


**Figure 8.** Pt<sub>3</sub>Co cathode catalysts normalized ECA loss (a), normalized mass activity (M.A.) loss (b) and H<sub>2</sub>/Air performance loss at 0.8 A/cm<sup>2</sup> (c) and 1.5 A/cm<sup>2</sup> (d) under extreme operating conditions after 0.4–0.95 V square wave cycling (20 sec/cycle).

Performance decay to 10,000 cycles for the parametric study at 0.8 A/cm<sup>2</sup> and 1.5 A/cm<sup>2</sup> in H<sub>2</sub>/Air is shown in Figure 8c,d respectively, with corresponding ECA and mass activity losses provided in Figure 8a,b. In general, ECA is still declining for all conditions after 5000 cycles. Comparing the ECA and mass activity decay curves, it can be noted that while the 90 °C operation was more detrimental to ECA than the baseline conditions, the mass activity losses were comparable for these two conditions. While ECA loss reflects catalyst changes due to particle growth and Pt loss into the membrane, mass activity loss is also affected by changes in the intrinsic ORR activity of the electrochemically-active surfaces due to catalyst re-structuring and a decrease in the influence of Co on ORR activity (e.g., a loss of Co from the near-surface region of the particles. Comparing Figure 9b and 9c, the mass activity decay trends are similar to performance decay trends in the kinetic region, 0.8 A/cm<sup>2</sup>. Higher temperature and baseline (80 °C) showed about the same performance loss in the kinetic region (0.8 A/cm<sup>2</sup>) compared to stable performance for 30% RH and greater performance loss for 1.05 V upper potential limit. In this study, higher temperature resulted in greater performance decay in the mass transport region as compared to the baseline conditions. The 30% RH condition shows the least performance decay with minimal ECA loss and moderate mass activity loss. It is speculated that the low ionomer hydration at 30% RH restricts Pt<sup>2+/4+</sup> or Co<sup>n+</sup> generation/diffusion and thereby limits Pt Ostwald ripening, loss of Pt into the membrane, and ionomer contamination within the cathode and membrane. Several studies have reported the acceleration of carbon corrosion and Pt dissolution at potentials >0.95V [43].

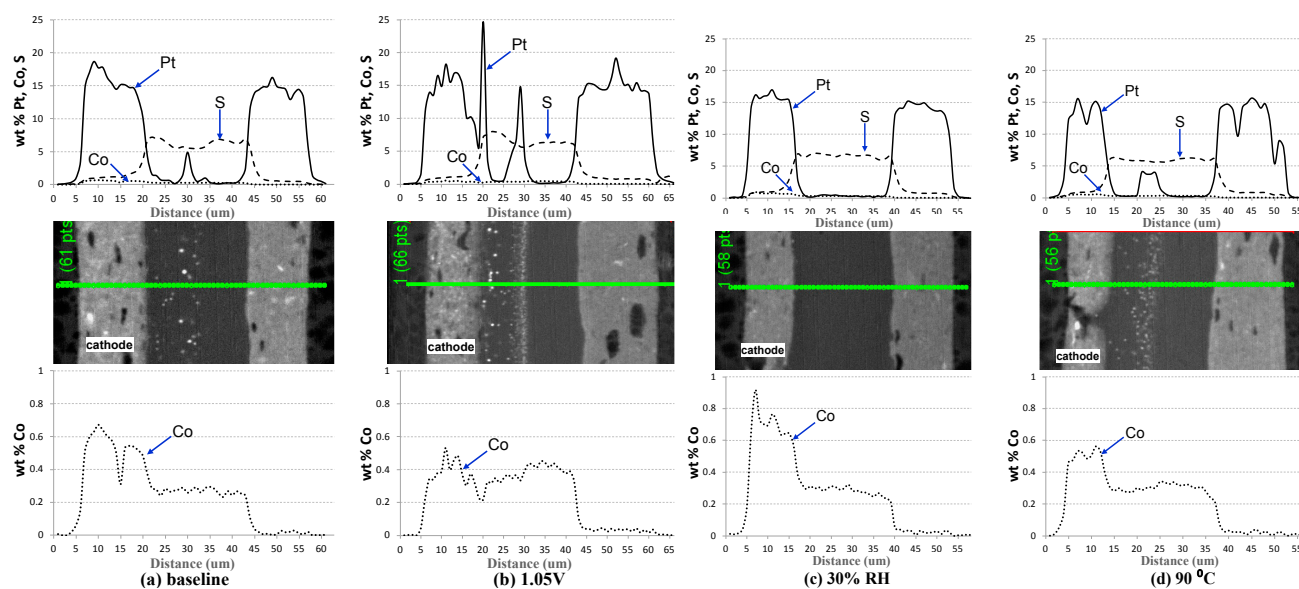


**Figure 9.** Post-test analysis of Pt<sub>3</sub>Co parametric operational study at subscale plan form midpoint consists of cross-section back-scattered SEM images and corresponding Pt, Co and S elemental profiles taken along lines indicated. (a) Baseline, (b) Higher upper potential (1.05 V), (c) Lower RH (30%) and (d) Higher Temperature (90 °C).

The post-test cross-section microscopy and Pt, Co and S profiling shown in Figure 9 indicate that Pt dissolution-deposition occurred extensively near the cathode side of the membrane for all conditions, except for 30% RH. It should be noted that Pt<sup>2+/4+</sup> generated during the parametric studies diffuses out of the cathode a farther distance into the membrane before being reduced to metallic Pt by crossover H<sub>2</sub>

than during the particle size study due to lower H<sub>2</sub> diffusion rate for 4% H<sub>2</sub> (balance N<sub>2</sub>) on the anode compared to 100% H<sub>2</sub> on the anode used for particle size study. Co mapping is also shown in the figure for the four MEAs. The wt.% Co<sup>n+</sup> in the membranes was in the order 1.05 V > 90 °C > baseline ≈ 30% RH.

For 90 °C condition, both higher diffusion rate of H<sub>2</sub> from the anode and faster deposition kinetics account for the denser focused Pt band in the membrane than the more diffused band for the baseline and high upper potential limit conditions. Ostwald ripening occurred for the 1.05 V condition as indicated by bright Pt spots within the cathode in back-scattered cross-section image, Figure 9b. Bright spots in the membrane seen for both the baseline and 1.05 V cells are indicative of growth of Pt deposits into large Pt particles from Pt<sup>2+/4+</sup> dissolution-migration-deposition from the cathode. Lastly, accelerated carbon corrosion at 1.05 V may also promote Pt particle migration and coalescence into large aggregate clusters within the cathode electrode. Losses in ECA and mass activity from Pt migration into the membrane for the 90 °C and 1.05 V cells could play significant role in performance decay, especially in the mass transport limited region, 1.5 A/cm<sup>2</sup>.

The Pt to Co atomic ratios in the cathodes of the four parametric-study cycled MEAs, as determined by XRF, are shown in Table 5. The trends in Co loss from the cathodes are 30% RH < Baseline ≈ 90 °C << 1.05 V. The trends in mass activity decay, Figure 8b, reflect these trends in impact of operating conditions on Co loss from the catalysts indicating that one of the primary sources of performance loss is catalyst restructuring. Using the same assumptions as described in the particle size study section, the depth of de-alloying was calculated to range from two to three monolayers for the 30% RH, baseline, and 90 °C cells and greater than three monolayers for the 1.05 V cell. This illustrates the destructive impact of increasing upper potential limits of cycling on the catalyst structure. Increased rates of Pt dissolution when cycling to upper potentials limits >1.0 V in aqueous electrolyte have been noted for polycrystalline Pt and Pt<sub>3</sub>Co nanoparticle catalysts [44–47]. The increased extent of Pt dissolution and/or the multi-layer structure of the oxide formed at these higher potentials [48,49] may expose additional Co in the sub-surface layers to the acidic environment resulting in an increased depth of de-alloying.

To gain greater insights into the observed decay trends of the 4.9 nm Pt<sub>3</sub>Co MEAs with varied operating conditions, the TEM-based catalyst particle size distribution analysis of the pre- and post-cycling electrodes is shown in Figure 10. All parametric conditions caused an increase in the mean diameter of the catalyst particles and an increasing in the tailing of the particle size distributions toward larger diameters. The extent of changes in the TEM particle size distributions are 30% RH < BL < 90 °C < 1.05 V. The trends agree with the ECA loss trends shown in Figure 8a. A quantitative comparison of the parametric decay trends between the Pt and Pt<sub>3</sub>Co alloys is not attempted, due to the size difference in the catalyst particles (3.2 nm for pure Pt [35] and 4.9 nm for Pt<sub>3</sub>Co), however, the qualitative trends are similar with no noticeable difference.

**Table 5.** The post-cycling Pt to Co ratios in the electrodes of the cells subjected to the parametric study square wave decay protocol.

Cell #	Description	Pt/Co Ratio
4	Baseline (BL)	7.8
5	Lower RH (30% RH)	6.6
6	Higher Upper Potential (1.05 V)	10.2
7	Higher Temperature (90 °C)	7.9

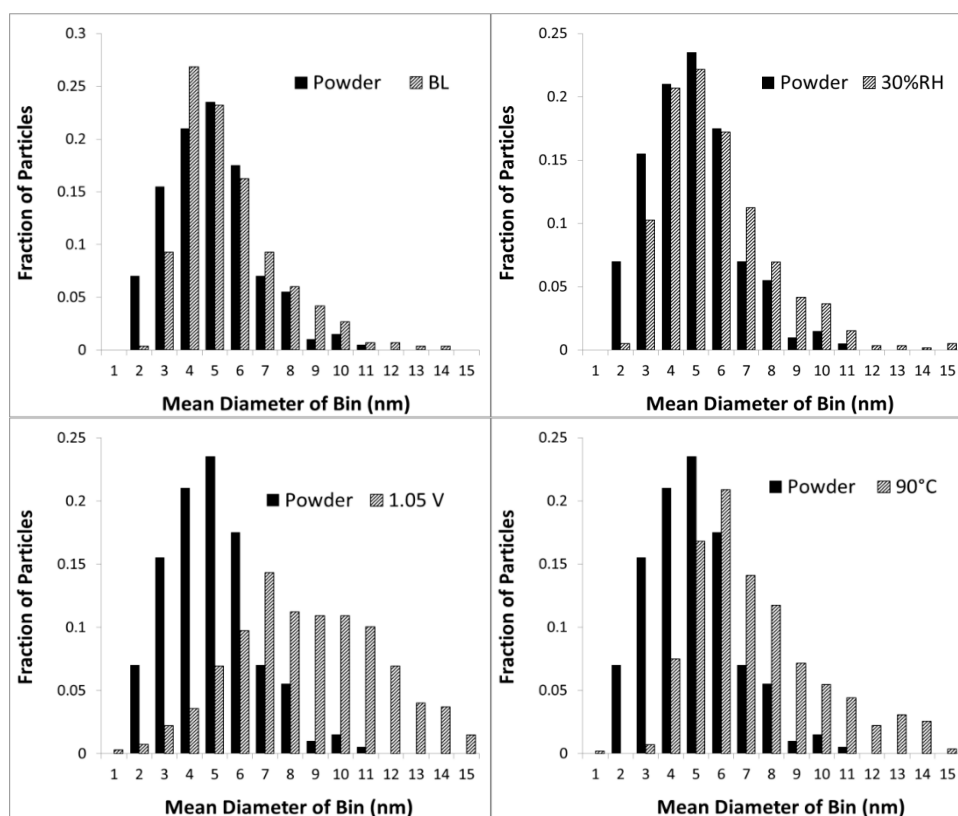


**Figure 10.** TEM analysis of Pt<sub>3</sub>Co particle size distributions of the pristine (**black**) and decayed catalysts (**hashed**) from parametric studies.

### 3. Experimental Section

#### 3.1. Catalyst Preparation

Catalysts were prepared by deposition of 40 wt.% Pt and Co (3:1 atomic ratio) on Akzo nobel Ketjen EC300J (Amsterdam, The Netherlands) via proprietary methods, then annealed at increasing temperatures (T1, T2 and T3) to achieve alloying and produce catalysts of specific particle sizes. Catalysts were characterized for total metal content by inductively-coupled plasma optical emission spectroscopy (ICP-OES) and X-ray fluorescence and metal surface area by gas-phase CO chemisorption. The results of these characterizations are summarized in Table 1. Powder X-ray diffraction (XRD), using a Bruker AXS D-500 diffractometer (Billerica, MA, USA) with a Cu K $\alpha$  X-ray source, was used to determine the average Pt<sub>3</sub>Co crystallite size (calculated using peak fitting and Rietveld analysis) and degree of alloying (shift in lattice parameter). The results of the XRD analysis are

also summarized in Table 1. In some cases, the catalyst was pre-leached to remove the easily leachable Co. Pre-leaching was carried out by chemically treating the Pt<sub>3</sub>Co/Ketjen EC 300J catalysts in air-saturated 0.5 M H<sub>2</sub>SO<sub>4</sub> at 363 K for 24 h. The metal content of the leached materials was determined via ICP-OES analysis.

### 3.2. Transmission Electron Microscopy (TEM) Characterization of Pt<sub>3</sub>Co/C Catalysts Annealed to Various Particle Sizes

A small portion of Pt<sub>3</sub>Co/C catalyst was crushed and dusted onto a holey carbon film on a Cu TEM grid. The samples were analyzed using a JEOL 2010F TEM operated (Peabody, MA, USA) at 200 kV. Energy Dispersive X-ray (EDX) analysis was used to confirm the Pt and Co composition. Particle size distributions were determined from at least 200 particles using a procedure described elsewhere [50]. Figure 11 shows TEM bright-field images of 40 wt.% Pt<sub>3</sub>Co/Ketjen EC 300J versions annealed at increasing temperatures (T1, T2 and T3) to generate larger average particle sizes.

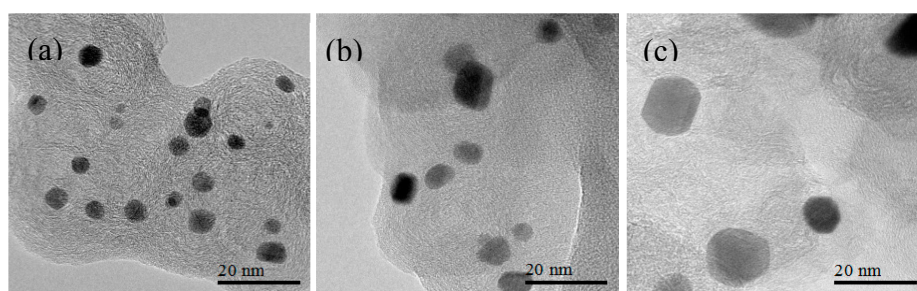


**Figure 11.** TEM bright-field images of as prepared (a) 4.9 nm (b) 8.1 nm and (c) 14.8 nm Pt<sub>3</sub>Co cathode catalysts supported on carbon (Scale bar = 20 nm).

The particle size distributions are summarized in Figure 12, where the bin frequency has been chosen such that all samples can be compared on the same plot. More detailed particle size distribution analysis for individual samples showed mono-modal log normal distributions for all three 40 wt.% Pt<sub>3</sub>Co/Ketjen EC 300J materials. Mean particle sizes were calculated from these images and are shown in Table 1.

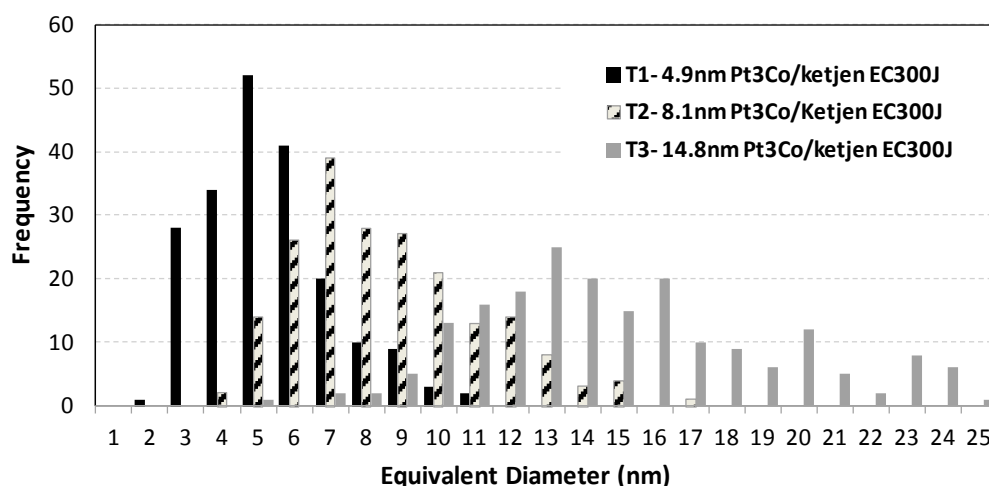


**Figure 12.** Particle size distributions of annealed Pt<sub>3</sub>Co cathode catalysts determined by TEM.

### 3.3. Membrane Electrode Assembly (MEA)

In this study, MEAs were fabricated via a developmental process, with identical anode Pt/Ketjen EC 300J catalyst, 35.6 wt.% Pt/C (~2 nm Pt particle size) and the same 25  $\mu\text{m}$  thickness perfluorosulfonic acid (PFSA) membrane. The cathode catalysts were the Pt<sub>3</sub>Co/Ketjen EC 300J materials described in Table 1. Cathode electrodes all had the same Pt loading of  $0.2 \text{ mg} \pm 0.02 \text{ mg Pt/cm}^2$  while the anode electrodes had a similar loading of  $0.22 \text{ mg} \pm 0.05 \text{ mg Pt/cm}^2$ .

### 3.4. Fuel Cell Construction

The MEA performance and durability tests utilized a 25  $\text{cm}^2$  active area fuel cell test fixture from Fuel Cell Technologies Inc. (Albuquerque, NM, USA). Prior to assembly in this fixture, the MEA was sandwiched between anode and cathode gas diffusion layers (GDLs) consisting of porous carbon paper coated on one side with a micro-porous layer (SGL25BC, SGL Group, Wiesbaden, Germany). This cell was then assembled between anode and cathode current collectors that had superimposed serpentine flow channels. The inlet and outlet was configured for co-flow of reactant gases. The assembled single cell was tested for cell resistance, gas crossover, and leakage. Subsequently, the cell was conditioned by scanning the current between 0.1 and 1.5  $\text{A/cm}^2$ , in 0.1  $\text{A/cm}^2$  increments every 5 min, for 16 h. The cell was maintained at 80  $^\circ\text{C}$  and operated at 101 kPa pressure (absolute) and 100% relative humidity (RH). The conditioning scans were performed by alternating between H<sub>2</sub>/Air and H<sub>2</sub>/O<sub>2</sub> reactant flows, corresponding to 50% utilization (or 0.05 SPLM as minimum flow rates) on both sides.

### 3.5. Diagnostics and V-I Performance

Diagnostic tests to determine electrochemically-active surface area (ECA) and ORR mass activity (A/g-Pt at 0.9 V) are commonly used to characterize cathode catalyst degradation. Decreases in ECA and mass activity are indicative of Pt nanoparticle growth and Pt<sup>2+/4+</sup> ion migration and deposition within the cathode or membrane ionomer. Microscopic post-test analysis was used to assess which Pt re-distribution processes dominate for the various standard and accelerated degradation protocols utilized in this study.

### 3.6. Hydrogen Crossover

Molecular H<sub>2</sub> crossover rate from anode to cathode of the MEAs was measured with H<sub>2</sub> on anode and N<sub>2</sub> on cathode at 80  $^\circ\text{C}$ , 150 kPa (absolute). A positive linear sweep voltammogram was performed by scanning the potential of the cathode between 0 and 0.45 V (vs. anode) with a sweep rate of 1 mV/s. The magnitude of the oxidation current at 0.35 V (vs. anode) in the voltammogram was used to determine the H<sub>2</sub> crossover rate.

### 3.7. Electrochemically-Active Surface Area (ECA)

The ECA of the cathode was measured using a cyclic voltammogram (CV) between 0.03 V and 1.0 V (vs. anode). A sweep rate of 10 mV/s was used with 0.5 SLPM of 4% H<sub>2</sub> (balance nitrogen) flowing over the anode (as reference as well as counter electrode) and 0.5 SLPM of N<sub>2</sub> flowing over

the cathode (as working electrode) at 80 °C, 101 kPa (absolute). ECA values ( $\text{m}^2/\text{g-Pt}$ ) were calculated by integrating the hydrogen adsorption charge in the voltammogram (0.05 to 0.35 V), dividing by cell active area ( $\text{cm}^2$ ),  $210 \mu\text{C}/\text{cm}^2$  (theoretical hydrogen monolayer adsorption on Pt) and the cathode initial Pt loading ( $\text{mg-Pt}/\text{cm}^2$ ).

### 3.8. Cell Performance

Electrochemical performance of the MEAs, represented by a voltage-current (V-I) curve, was measured with an electronic load box (Model 890, Scribner Associates Inc., Southern Pines, NC, USA), by scanning current from the open circuit voltage (OCV) to  $1500 \text{ mA}/\text{cm}^2$  and back to the OCV. The cells were purged with  $\text{H}_2$  and  $\text{N}_2$  on the anode and cathode, respectively, to reduce the OCV to  $\sim 0.1 \text{ V}$  for  $\sim 10 \text{ min}$  right before each V-I curve measurement to minimize the effect of platinum oxide, formed on the cathode catalyst at high potentials, on the cell performance. The V-I data collected during the decreasing current scan are reported. To focus the results on the cathode electrode characteristics, the cell voltage corrected for the membrane's ohmic loss (measured by the current interrupt method), the so-called IR-corrected voltage, is reported. The IR-corrected polarization plots are useful for quantifying the kinetic, ohmic and mass transport behaviors of the electrode.

$\text{H}_2/\text{O}_2$  performance was measured at 80 °C and 150 kPa (absolute) with  $\text{H}_2$  on the anode and  $\text{O}_2$  on the cathode with flow rates corresponding to 50% utilization (or 0.05 SPLM as minimum flow rates) on both sides. Mass activity ( $\text{A}/\text{g-Pt}$ ) is the measured current ( $\text{A}/\text{cm}^2$ ) @ 0.9 V in IR-corrected  $\text{H}_2/\text{O}_2$  polarization plots, corrected by hydrogen crossover current ( $\text{A}/\text{cm}^2$ ) and then normalized to initial Pt loading ( $\text{g-Pt}/\text{cm}^2$ ) of cathode electrodes.

$\text{H}_2/\text{air}$  performance was measured at 80 °C, 150 kPa (absolute) with  $\text{H}_2$  on the anode and air on the cathode with flow rates of 1 SLPM and 2 SLPM, respectively.

### 3.9. Decay Protocol for Particle Size Studies

Accelerated cell degradation cycling protocols were imposed on the MEAs using a potentiostat (EG&G 273A, Princeton Applied Research Inc., Oak Ridge, TN, USA). The decay conditions are provided in Table 2. To elucidate the effect of cathode catalyst particle size on performance degradation, MEAs containing the three  $\text{Pt}_3\text{Co}$  cathode catalysts were subjected to a triangle-wave potential cycle between 0.6 V and 1.0 V with 50 mV/s ramp rate (16 s/cycle). The cells were maintained at 80 °C and had fixed gas flows of 0.1 SLPM  $\text{H}_2$  on the anode and 0.05 SLPM  $\text{N}_2$  on the cathode, both at 100% RH. During the potential cycling, the cathode served as working electrode, while the anode served as both reference and counter electrode. The cyclic decay tests were paused at specific intervals to evaluate the cathode ECA and cell V-I performance.

### 3.10. Decay Protocol for Parametric Studies

The accelerated cell degradation test conditions to elucidate the effects of cell operating parameters on MEAs containing the 4.9 nm mean diameter  $\text{Pt}_3\text{Co}$  cathode catalyst are shown in Table 3. A square-wave potential cycle with 20 s/cycle was imposed on the cell, using a potentiostat, at defined temperature, RH and voltage window conditions for 10,000 cycles. Fixed gas flows of 0.5 SLPM 4%  $\text{H}_2$

(balance N<sub>2</sub>) on anode and 0.5 SLPM N<sub>2</sub> on cathode were used. A new MEA with 4.9 nm mean particle size Pt<sub>3</sub>Co cathode catalyst was used for each test to evaluate the impact of one parametric condition (high temperature, low RH, or higher upper potential limit) on cell decay behavior. During the potential cycling, the cathode served as working electrode, while the anode served as both reference and counter electrode. The cyclic decay tests were paused at specific intervals to evaluate the cathode ECA and cell V-I performance.

### 3.11. Electron MicroProbe Analysis (EMPA)

Narrow strips (~5 mm wide) were cut down the midline from the inlet to the outlet from pristine and decayed MEAs (5 cm × 5 cm active area) for cross-section microscopic analysis. The MEA strips were set into epoxy resin, polished, surface-coated with a uniform thin layer of carbon for electron microprobe analysis by a JEOL 8900 Super Probe (Peabody, MA, USA) equipped with a multiple wave length dispersive spectrometer (WDS) for simultaneous profiling of Pt, Co, and S distribution across the MEA cross-sections.

### 3.12. X-ray Fluorescence Analysis (XRF)

Portions of the cathode catalyst were removed from narrow strips of the fresh and decayed MEAs, identical to those used for EMPA, using adhesive tape. The atomic ratio of Pt to Co in these catalyst samples were analyzed utilizing an Energy-Dispersive X-ray Fluorescence Spectrometer (Rigaku NEX CG EDXRF Analyzer with Polarization, The Woodlands, TX, USA), the copper and molybdenum targets of the spectrometer, and empirical fitting using the integrated intensity of the Pt L and the Co K.

## 4. Conclusions

Electrochemical decay protocols were used to accelerate performance loss of Pt<sub>3</sub>Co catalyst based electrodes with three distinct mean particle sizes. The decay trends observed for the Pt<sub>3</sub>Co alloy particles is compared with that of the similar study reported on platinum particles [36]. Over the broad range of particle sizes evaluated for the first time, a clear trend is emerging. While the initial performance of the smaller particle based catalysts is higher, the durability of the larger particle based catalysts is higher. The intermediate particle sizes of ~5 nm for Pt and ~8 nm for Pt<sub>3</sub>Co catalysts seems to provide the best life averaged performance. Furthermore, it is interesting that in the current study the 5 nm size Pt catalyst based electrodes exhibited comparable mass activity as that of 4.9 nm Pt<sub>3</sub>Co catalyst based electrodes and the durability is also comparable. This result is rather unexpected, as the literature trends suggest improved mass activity with alloying. The heat treatment conditions during catalyst preparation, catalyst ink preparation and MEA fabrication may have an important role to play in realizing the initial mass activity benefits reported in literature. The fraction of Co leached into the membrane is shown to be a function of the particle size and is lowest for the larger particle size.

The impact of operating conditions on the durability of the 4.9 nm Pt<sub>3</sub>Co alloy catalyst based electrodes is also reported. The order of performance decay based on operational conditions, from greatest to least, for the parametric study was 1.05 V upper limit >> 90 °C > baseline > 30% RH.

In addition to this qualitative trend, the approaches used are able to quantify the extent of catalyst damage incurred due to the fuel cell operation and the choice of catalysts used.

### Acknowledgments

This work was performed under the DOE contract DE-AC02-06CH11357.

### Author Contributions

Sarah Ball carried out the preparation of catalysts and MEAs, contributed to the characterization of catalyst powders. Zhiwei Yang and Mallika Gummalla performed the MEAs' in-cell tests and post-test EMPA analysis. Somaye Rasouli, Kang Yu and Paulo Ferreira carried out the TEM and XRD analysis. Deborah Myers performed the XRF measurements. All the authors contributed equally to the data interpretation and discussion. Mallika Gummalla and David Condit drafted the manuscript, and Deborah Myers and Zhiwei Yang revised the final version of paper.

### Conflicts of Interest

The authors declare no conflict of interest.

### References

1. Ball, S.C.; Hudson, S.L.; Theobald, B.R.C.; Thompsett, D. PtCo, a Durable Catalyst for Automotive PEMFC. *ECS Trans.* **2007**, *11*, 1267–1278.
2. Stamenkovic, V.R.; Mun, B.S.; Arenz, M.; Mayrhofer, K.J.J.; Lucas, C.A.; Wang, G.; Ross, P.N.; Markovic, N.M. Trends in Electrocatalysis on Extended and Nanoscale Pt-Bimetallic Alloy Surfaces. *Nat. Mater.* **2007**, *6*, 241–247.
3. Colón-Mercado, H.R.; Popov, B.N. Stability of Platinum Based Alloy Cathode Catalysts in PEM Fuel Cells. *J. Power Sources* **2006**, *155*, 253–263.
4. Stamenkovic, V.R.; Fowler, B.; Mun, B.S.; Wang, G.; Ross, P.N.; Lucas, C.A.; Markovic, N.M. Improved Oxygen Reduction Activity on Pt<sub>3</sub>Ni(111) via Increased Surface Site Availability. *Science* **2007**, *315*, 493–497.
5. Van der Vliet, D.F.; Wang, C.; Tripkovic, D.; Strmcnik, D.; Zhang, X.; Debe, M.K.; Atanasoski, R.T.; Markovic, N.M.; Stamenkovic, V.R. Mesoporous Thin Films as Electrocatalysts with Tunable Composition and Surface Morphology. *Nat. Mater.* **2012**, *11*, 1051–1058.
6. Wang, C.; van der Vliet, D.; Chang, K.; You, H.; Strmcnik, D.; Schlueter, J.A.; Markovic, N.M.; Stamenkovic, V.R. Monodisperse Pt<sub>3</sub>Co Nanoparticles as a Catalyst for the Oxygen Reduction Reaction: Size-Dependent Activity. *J. Phys. Chem.* **2009**, *113*, 19365–19368.
7. Paulusa, U.A.; Wokauna, A.; Scherera, G.G.; Schmidt, T.J.; Stamenkovic, V.; Markovic, N.M.; Ross, P.N. Oxygen Reduction on High Surface Area Pt-Based Alloy Catalysts in Comparison to Well Defined Smooth Bulk Alloy Electrodes. *Electrochem. Acta* **2002**, *47*, 3787–3798.
8. Huang, Y.; Zhang, J.; Kongkanand, A.; Wagner, F.T.; Li, J.C.M.; Jorné, J. Transient Platinum Oxide Formation and Oxygen Reduction on Carbon-Supported Platinum and Platinum-Cobalt Alloy Electrocatalysts. *J. Electrochem. Soc.* **2014**, *161*, F10–F15.

9. Stamenkovic, V.R.; Mun, B.S.; Mayrhofer, K.J.J.; Ross, P.N.; Markovic, N.M.; Rossmeisl, J.; Greeley, J.; Nørskov, J.K. Changing the Activity of Electrocatalysts for Oxygen Reduction by Tuning the Surface Electronic Structure. *Angew. Chem.* **2006**, *45*, 2897–2901.
10. Stamenkovic, V.R.; Mun, B.S.; Mayrhofer, K.J.J.; Ross, P.N.; Markovic, N.M. Effect of Surface Composition on Electronic Structure, Stability, and Electrocatalytic Properties of Pt-Transition Metal Alloys: Pt-Skin versus Pt-Skeleton Surfaces. *J. Am. Chem. Soc.* **2006**, *128*, 8813–8819.
11. Jalan, V.; Taylor, E.J. Importance of Interatomic Spacing in Catalytic Reduction of Oxygen in Phosphoric Acid. *J. Electrochem. Soc.* **1983**, *130*, 2299–2302.
12. Toda, T.; Igarashi, H.; Uchida, H.; Watanabe, M. Enhancement of the Electroreduction of Oxygen on Pt Alloys with Fe, Ni, and Co. *J. Electrochem. Soc.* **1999**, *146*, 3750–3756.
13. Min, M.K.; Cho, J.; Cho, K.; Kim, H. Particle size and Alloying Effects of Pt-Based Alloy Catalysts for Fuel Cell Applications. *Electrochem. Acta* **2000**, *45*, 4211–4217.
14. Mukerjee, S.; Srinivasan, S.; Soriaga, M.; McBreen, J. Role of Structural and Electronic Properties of Pt and Pt Alloys on Electrocatalysis of Oxygen Reduction an *in situ* XANES and EXAFS Investigation. *J. Electrochem. Soc.* **1995**, *142*, 1409–1422.
15. Roques, J.; Anderson, A.B.; Murthi, V.S.; Mukerjee, S. Potential Shift for OH<sub>ads</sub> Formation on the Pt Skin on Pt<sub>3</sub>Co (111) Electrodes in Acid. *J. Electrochem. Soc.* **2005**, *152*, E193–E199.
16. Dubau, L.; Maillard, F.; Chatenet, M.; Guetaz, L.; André, J.; Rossinot, E. Durability of Pt<sub>3</sub>Co/C Cathodes in a 16 Cell PEMFC Stack: Macro/Microstructural Changes and Degradation Mechanisms. *J. Electrochem. Soc.* **2010**, *157*, B1887–B1895.
17. Dubau, L.; Lopez-Haroa, M.; Castanheira, L.; Dursta, J.; Chateneta, M.; Bayle-Guillemaudb, P.; Guétazc, L.; Caquéd, N.; Rossinotd E.; Maillard, F. Probing the Structure, the Composition and the ORR Activity of Pt<sub>3</sub>Co/C nanocrystallites during a 3422 h PEMFC Ageing Test. *Appl. Catal. B* **2013**, *142–143*, 801–808.
18. Chen, S.; Gasteiger, H.A.; Hayakawa, K.; Tada, T.; Yang, S. Platinum-Alloy Cathode Catalyst Degradation in Proton Exchange Membrane Fuel Cells: Nanometer-Scale Compositional and Morphological Changes. *J. Electrochem. Soc.* **2010**, *157*, A82–A97.
19. Shao, M.; Peles, A.; Shoemaker, K. Electrocatalysis on Platinum Nanoparticles: Particle Size Effect on Oxygen Reduction Reaction Activity. *Nano Letters* **2011**, *11*, 3714–3719.
20. Kinoshita, K. Particle Size Effects for Oxygen Reduction on Highly Dispersed Platinum in Acid Electrolytes. *J. Electrochem. Soc.* **1990**, *137*, 845–848.
21. Han, B.C.; Miranda, C.R.; Ceder, G. Effect of Particle Size and Surface Structure on Adsorption of O and OH on Platinum Nanoparticles: A First-Principles Study. *Phys. Rev.* **2008**, *B77*, 075410.
22. Tritsarlis, G.A.; Greeley, J.; Rossmeisl, J.; Nørskov, J.K. Atomic-Scale Modeling of Particle Size Effects for the Oxygen Reduction Reaction on Pt. *Catal. Lett.* **2011**, *141*, 909–913.
23. Wang, D.; Xin, H.L.; Hovden, R.; Wang, H.; Yu, Y.; Muller, D.A.; DiSalvo, F.J.; Abruña, H.D. Structurally Ordered Intermetallic Platinum-Cobalt Core-Shell Nanoparticles with Enhanced Activity and Stability as Oxygen Reduction Electrocatalysts. *Nat. Mater.* **2013**, *12*, 81–87.
24. Chen, S.; Sheng, W.; Yabuuchi, N.; Ferreira, P.J.; Allard, L.F.; Yang, S. Origin of Oxygen Reduction Reaction Activity on “Pt<sub>3</sub>Co” Nanoparticles: Atomically Resolved Chemical Compositions and Structures. *J. Phys. Chem. C* **2009**, *113*, 1109–1125.

25. Gasteiger, H.A.; Kocha, S.S.; Sompalli, B.; Wagner, F.T. Activity Benchmarks and Requirements for Pt, Pt-Alloy, and Non-Pt Oxygen Reduction Catalysts for PEMFCs. *Appl. Catal. B* **2005**, *56*, 9–35.
26. Nesselberger, M.; Ashton, S.; Meier, J.C.; Katsounaros, I.; Mayrhofer, K.J.J.; Arenz, M. The Particle Size Effect on the Oxygen Reduction Reaction Activity of Pt Catalysts: Influence of Electrolyte and Relation to Single Crystal Models. *J. Am. Chem. Soc.* **2011**, *133*, 17428–17433.
27. Mayrhofer, K.J.J.; Blizanac, B.B.; Arenz, M.; Stamenkovic, V.R.; Ross, P.N.; Markovic, N.M. The Impact of Geometric and Surface Electronic Properties of Pt-Catalysts on the Particle Size Effect in Electrocatalysis. *J. Phys. Chem. B* **2005**, *109*, 14433–14440.
28. Aindow, T.T.; Bi, W.; Izzo, E.; Motupally, S.; Murthi, V.S.; Perez-Acosta, C. Structure-Activity-Durability relationship of Pt and Pt based Alloy Electrocatalysts. In Proceedings of 215th Meeting of the Electrochemical Society, San Francisco, CA, USA, 24–29 May 2009.
29. Bi, W.; Izzo, E.; Murthi, V.S.; Perez-Acosta, C.; Lisitano, J.; Protsailo, L.V. Durability of Low Temperature Hydrogen PEM Fuel Cells with Pt and Pt Alloy ORR Catalysts. In Proceedings of 218th Meeting of the Electrochemical Society, Las Vegas, NV, USA, 10–15 October 2010.
30. Matsutani, K.; Hayakawa, K.; Tada, T. Effect of Particle Size of Platinum and Platinum-Cobalt Catalysts on Stability against Load Cycling. *Platin. Met. Rev.* **2010**, *54*, 223–232.
31. Strasser, P.; Koh, S.; Anniyev, T.; Greeley, J.; More, K.; Yu, C.; Liu, Z.; Kaya, S.; Nordlund, D.; Ogasawara, H.; Toney, M.F.; Nilsson, A. Lattice-Strain Control of the Activity in Dealloyed Core-Shell Fuel Cell Catalysts. *Nat. Chem.* **2010**, *2*, 454–460.
32. Adzic, R.R.; Zhang, J.; Sasaki, K.; Vukmirovic, M.B.; Shao, M.; Wang, J.X.; Nilekar, A.U.; Mavrikakis, M.; Valerio, J.A.; Uribe, F. Platinum Monolayer Fuel Cell Electrocatalysts. *Top. Catal.* **2007**, *46*, 249–262.
33. Vukmirovic, M.B.; Zhang, J.; Sasaki, K.; Uribe, F.; Mavrikakis, M.; Adzic, R.R. Platinum Monolayer Electrocatalysts for Oxygen Reduction. *Electrochem. Acta* **2007**, *52*, 2257–2263.
34. Sasaki, K.; Wang, J.X.; Naohara, H.; Marinkovic, N.; More, K.; Inada, H.; Adzic, R.R. Recent Advances in Platinum Monolayer Electrocatalysts for Oxygen Reduction Reaction: Scale-up Synthesis, Structure and Activity of Pt Shells on Pd Cores. *Electrochem. Acta* **2010**, *55*, 2645–2652.
35. Yang, Z.; Ball, S.C.; Condit, D.A.; Gummalla, M. Systematic Study on the Impact of Pt Particle Size and Operating Conditions on PEMFC Cathode Catalyst Durability. *J. Electrochem. Soc.* **2011**, *158*, B1439–B1445.
36. Carter, R.N.; Kocha, S.S.; Wagner, F.; Fay, M.; Gasteiger, H.A. Artifacts in Measuring Electrode Catalyst Area of Fuel Cells through Cyclic Voltammetry. *ECS Trans.* **2007**, *11*, 403–410.
37. Shao, M.; Odell, J.H.; Choi, S.; Xia, Y. Electrochemical Surface Area Measurements of Platinum- and Palladium-Based Nanoparticles. *Electrochem. Commun.* **2013**, *31*, 46–48.
38. Van der Vliet, D.F.; Wang, C.; Li, D.; Paulikas, A.P.; Greeley, J.; Rankin, R.B.; Strmcnik, D.; Tripkovic, D.; Markovic, N.M.; Stamenkovic, V.R. Unique Electrochemical Adsorption Properties of Pt-Skin Surfaces. *Angew. Chem.* **2012**, *51*, 3139–3142.
39. Yan, Q.; Wu, J. Modeling of Single Catalyst Particle in Cathode of PEM Fuel Cells. *Energy Convers. Manage.* **2008**, *49*, 2425–2433.

40. Greszler, T.A.; Moylan, T.E.; Gasteiger, H.A. Modeling the Impact of Cation Contamination in a Polymer Electrolyte Membrane Fuel Cell. *Handbook of Fuel Cells—Fundamentals, Technology and Applications*; John Wiley & Sons Ltd.: Chichester, UK, 2009.
41. Chen, S.; Ferreira, P.J.; Sheng, W.; Yabuuchi, N.; Allard, L.; Yang, S., Enhanced Activity for Oxygen Reduction Reaction on “Pt<sub>3</sub>Co” Nanoparticles: Direct Evidence of Percolated and Sandwich-Segregation Structures. *J. Am. Chem. Soc.* **2008**, *130*, 13818–13819.
42. Carlton, C.E.; Chen, S.; Ferreira, P.J.; Allard, L.F.; Yang, S. Sub-Nanometer-Resolution Elemental Mapping of “Pt<sub>3</sub>Co” Nanoparticle Catalyst Degradation in Proton-Exchange Membrane Fuel Cells. *J. Phys. Chem. Lett.* **2012**, *3*, 161–166.
43. Yang, S., Sheng, W.C.; Chen, S.; Ferreira, P.J.; Holby, E.F.; Morgan, D. Instability of Supported Platinum Nanoparticles in Low-Temperature Fuel Cells. *Top. Catal.* **2007**, *46*, 285–305.
44. Kinoshita, K.; Lundquist, J.T.; Stonehart, P.J. Potential Cycling Effects on Platinum Electrocatalyst Surfaces. *J. Electroanal. Chem. Interfacial Electrochem.* **1973**, *48*, 157–166.
45. Rand, D.A.J.; Woods, R.J.A Study of the Dissolution of Platinum, Palladium, Rhodium and Gold Electrodes in 1 m Sulphuric Acid by Cyclic Voltammetry. *J. Electroanal. Chem. Interfacial Electrochem.* **1972**, *35*, 209–218.
46. Wang, X.; Myers, D.J.; Kariuki, N.; Kumar, R. Dissolution of Platinum and Platinum Alloy PEFC Cathode Electrocatalysts. In Proceedings of 211th Meeting of the Electrochemical Society, Chicago, Illinois, USA, 6–10 May 2007.
47. Wang, X.; Myers, D.J.; Smith, M.C.; Mawdsley, J.; Kumar, R. Dissolution of Platinum-based PEFC Cathode Electrocatalysts. In Proceedings of 214th Meeting of the Electrochemical Society, Honolulu, HI, USA, 12–17 October 2008.
48. Teliska, M.; O’Grady, W.E.; Ramaker, D.E. Determination of O and OH Adsorption Sites and Coverage *in situ* on Pt Electrodes from PtL<sub>23</sub> X-ray Absorption Spectroscopy. *J. Phys. Chem. B* **2005**, *109*, 8076–8084.
49. Imai, H.; Izumi, K.; Matsumoto, M.; Kubo, Y.; Kato K.; Imai, Y. *In situ* and Real-Time Monitoring of Oxide Growth in a Few Monolayers at Surfaces of Platinum Nanoparticles in Aqueous Media. *J. Am. Chem. Soc.* **2009**, *131*, 6293–6300.
50. Groom, D.J. The Effect of Nanocatalyst Size on Performance and Degradation in the Cathode of Proton Exchange Membrane Fuel Cells. M.S. Thesis, University of Texas at Austin, December 2011.